Letter

Two-dimensional crystal structure of aquaporin-4 bound to the inhibitor acetazolamide

Akiko Kamegawa[1], Yoko Hiroaki[2], Kazutoshi Tani[2],*, and Yoshinori Fujiyoshi[1,2],*

[1]Graduate School of Pharmaceutical Sciences, Nagoya University, Nagoya 464-8601, Japan, and
[2]Cellular and Structural Physiology Institute, Nagoya University, Nagoya 464-8601, Japan

*To whom correspondence should be addressed. E-mail: tani@cespi.nagoya-u.ac.jp (K.T.)/yoshi@cespi.nagoya-u.ac.jp (Y.F.)

Abstract

Acetazolamide (AZA) reduces the water permeability of aquaporin-4, the predominant water channel in the brain. We determined the structure of aquaporin-4 in the presence of AZA using electron crystallography. Most of the features of the 5-Å density map were consistent with those of the previously determined atomic model. The map showed a protruding density from near the extracellular pore entrance, which most likely represents the bound AZA. Molecular docking simulations supported the location of the protrusion as the likely AZA-binding site. These findings suggest that AZA reduces water conduction by obstructing the pathway at the extracellular entrance without inducing a large conformational change in the protein.

Key words: water channel, inhibitor bound structure, 2D crystal, electron microscopy, electron crystallography

Introduction

Almost all living cells regulate their water exchange in response to osmotic pressure. Water channels of the aquaporin (AQP) family achieve the diffusive water permeation required for biological function and form tetramers [1]. Since the discovery of the first water channel, AQP1 [2], more than 300 AQPs have been identified in many organisms from bacteria to plants and mammals. AQP family members are classified into two subfamilies: an AQP group that is highly selective for water, and an aquaglyceroporin group that allows both water and other small neutral solutes, like glycerol and urea, to permeate the membrane. Thirteen AQPs (AQP0 to 12) have been identified in mammals and 5 mammalian AQPs have been solved at atomic resolution [1,3,4]. The first atomic structure of human AQP1 was determined by electron crystallography

[5], which revealed the unique AQP fold with six transmembrane helices (termed H1–H6) and two short pore helices (termed HB and HE), together with the highly conserved Asn-Pro-Ala (NPA) motifs in the middle of the membrane. Each AQP monomer has a channel pore, and the individual pores work independently within a functional tetramer. In the channel pathway, the narrowest region, which is located between the NPA motif and the extracellular pore entrance, is called the ar/R (aromatic/arginine) constriction site [6]. In the AQP group, the width of the ar/R site is the same as the diameter of a water molecule [5].

AQP4 is a water selective channel that is predominantly expressed in the brain, but also expressed in other tissues [7]. There are three functional splicing isoforms of AQP4 and their expression ratio determines the size of the orthogonal arrays that AQP4 forms in the endfeet of astrocytes

[8,9]. The long AQP4 isoform with a full N-terminus start-ing with Met1 (AQP4M1) contains palmitoylated cysteines and thus sterically impedes the formation of arrays, whereas the short isoform starting with Met23 (AQP4M23) easily forms arrays due to the absence of palmitoylation sites [10]. A recently discovered functional isoform, AQP4e, has 41 residues extending from the N-terminus of AQP4M1. Its expression level is quite low in rat brain, but it transports water and has no ability to form arrays, similar to AQP4M1 [11,12]. The function of AQP4 arrays remains elusive, but the water permeability of functional isoforms is quite similar [11,13]. AQP4 has important roles in maintaining brain homeostasis [14] as well as in several brain patho-logies, including brain edema [15] and neuromyelitis optica [16].

Most AQPs are thought to be in a constitutively open conformation, but some water channels adopt a closed con-formation that is regulated by various mechanisms [3]. Among them, the spinach plasma membrane AQP SoPIP2;1 is a functionally and structurally well-studied AQP whose gating is regulated to protect the plant against drought or flood [17,18]. A plausible channel gating mechanism of SoPIP2;1 regulated by phosphorylation, pH or Ca^{2+} was proposed based on X-ray structural studies combined with molecular dynamics simulations [17]. The conformational changes in loop D mainly contribute to the central part of its gating. In the closed state, loop D forms an antiparallel β-sheet to cover the cytoplasmic pore entrance with the dis-placement of Leu197. In contrast, in the open state loop D does not adopt a secondary structure that is displaced to move away from the pore, and the N terminus of helix 5 extends into the cytoplasmic side. The model proposes that closure of the pore is stimulated by the dephosphorylation of two conserved serine residues (Ser115 or Ser274) or by protonation of a conserved histidine residue (His193). No experimental evidence to date, however, has demonstrated the phosphorylation of either Ser115 in SoPIP2;1 or a corre-sponding site in any other plant AQP. This together with other evidence contradicting the model [19–21] suggests that more information is needed to fully elucidate the gating mechanism regulated by phosphorylation. The water per-meability of mammalian AQP0 is affected by the pH, par-tially due to the protonation state of a His residue in loop A, and by Ca^{2+} in a calmodulin-dependent gating mechanism [3,22]. These mechanisms help to regulate osmotic pressure through AQPs in response to surrounding conditions and are tightly linked to the physiological functions of the cells that express the water channels. Mercury, silver and gold suppress the activities of several AQPs [23–26], but these elements are not suitable for clinical application due to their toxicity and non-specificity for AQPs. Many recent studies describing the application of AQP inhibitors for human

diseases have revealed the potential of AQPs as therapeutic targets [27].

Acetazolamide (AZA or AZM), a well-known carbonic anhydrase inhibitor, reduces the water permeability of AQP1 in *Xenopus laevis* oocytes [28]. AZA has also been reported to be an AQP4 inhibitor [29,30]. Some groups reported, however, that AZA does not affect the water per-meability of AQP1 in erythrocytes and AQP4 in brain glial cells [31–33]. Our previous studies using proteoliposomes indicated that AZA inhibits AQP4 activity, but has no effect on AQP1 [34]. The results of *in vitro* assays using proteoli-posomes are more reliable and reproducible than those obtained in assays using living cells, such as oocytes and mammalian cells, which may explain the discrepancy in the findings obtained with different systems. To investigate the structural effect of AZA binding, we determined the AQP4 structure in complex with AZA by electron crystallography at 5 Å resolution, and further validated the binding site using a molecular docking simulation study.

Materials and methods

Preparation of the constructs, and expression and purifica-tion procedures for rat AQP4M23 (rAQP4M23) were per-formed as previously described [35,36]. Purified protein was mixed with *Escherichia coli* total lipid extract (Avanti) at a lipid-to-protein ratio of 1.0 (w/w). The mixture was dia-lyzed in a dialysis button for 3 days against 10 mM MES (pH 6.0), 100 mM NaCl, 50 mM $MgCl_2$, 2 mM dithio-threitol and 1% glycerol. During dialysis, the temperature was maintained at 20°C on the first day, increased to 37°C on the second day and decreased again to 20°C on the third day. After harvesting, 2D crystals were soaked in the same dialysis buffer containing 1 mM AZA (Sigma-Aldrich), which was solvated with 0.05% *N,N*-dimethylformamide, and maintained at 20°C for 1–3 h.

Specimens for cryo-electron microscopy were prepared using the conventional single carbon film technique with molybdenum grids and a final trehalose concentration of 7% (w/v). Double-layered 2D crystals tended to be more slippery between layers in the presence of AZA than in the absence of AZA. The preparation using the carbon sand-wich technique drastically increased the failure rate of merging data to reconstruct the 3D structure. The slippery crystal effect was more severe than the charging-up effects. Thus, we chose the conventional technique to collect the images, although we had to take a lot of images to obtain good ones without an image shift. Electron micrographs were recorded with a JEM3000SFF electron microscope equipped with a liquid-helium stage [37,38] and a field-emission electron source with an acceleration voltage of 300 kV. Images of specimens were tilted at angles of 0, 20,

45 and 60°, and recorded on Kodak SO-163 film (Carestream Health) at a nominal magnification of 40 000× with a 2-s exposure time, corresponding to a total electron dose of 20 electron Å^{-2}. Micrographs were developed for 14 min using a full-strength Kodak D19 developer.

All digitized images were processed with modified versions of the MRC image processing programs [39]. The images were computationally unbent and corrected for the contrast transfer function (CTF) [40]. The initial CTF parameters for each image were determined as previously described [36]. The Fourier transform of each image diffracted around 5 Å resolution along the tilt axis (Fig. 1). Images from crystals of the predominant crystal type ($P42_12$) were merged and used to calculate a 3D density map at 5 Å resolution by applying a negative B-factor of -200 Å^2 (Figs. 2 and 3). The characteristics of our electron crystallographic structure of rAQP4M23 are summarized in Table 1. All figures were prepared using Chimera [41]. The
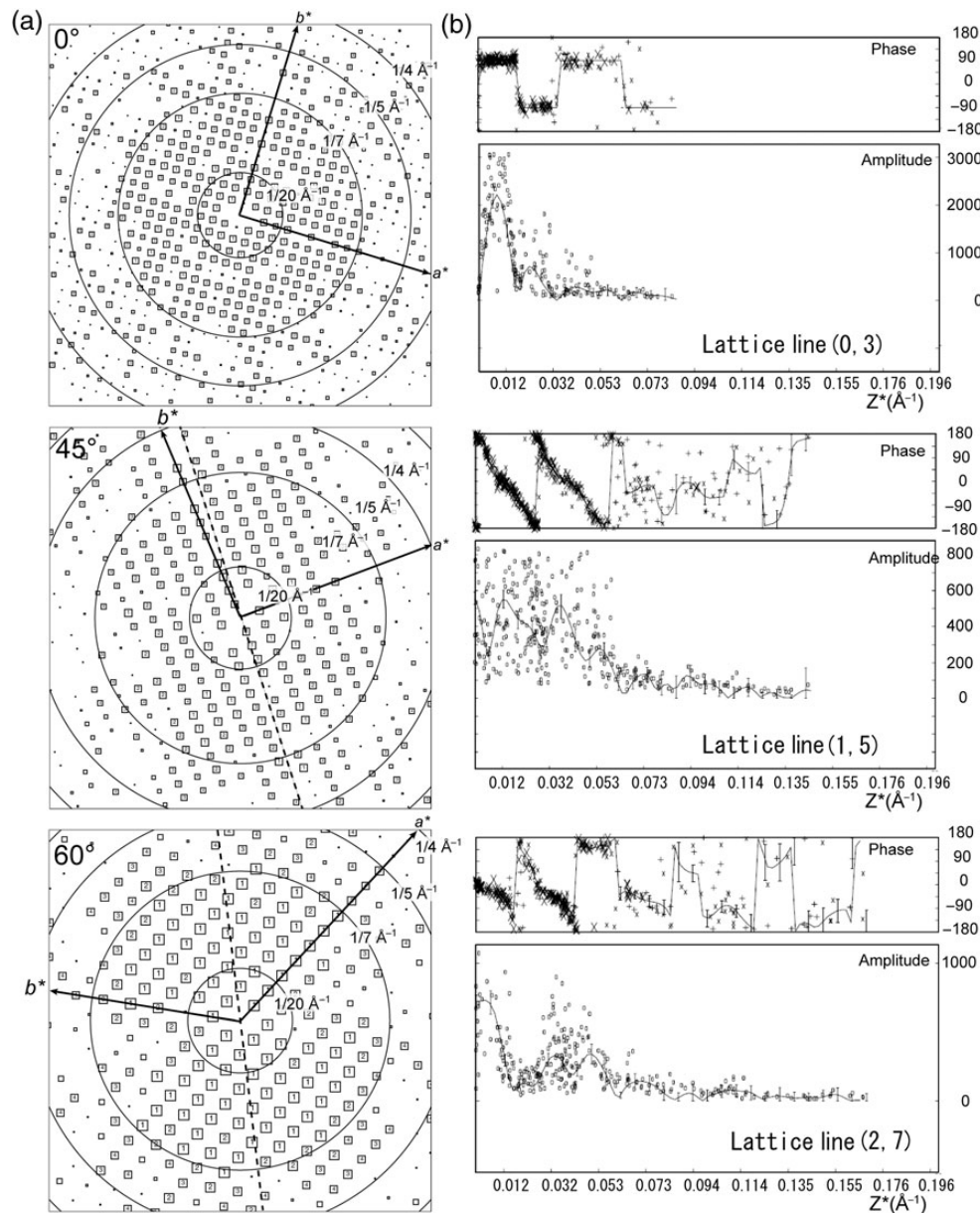
Fig. 1. IQ plots and lattice lines. (a) IQ [40] plots calculated from Fourier transforms of images of frozen-hydrated 2D crystals of AQP4 bound to AZA at tilt angles of 0, 45 and 60°. Circles with the label text in the upper right indicate resolutions of 20, 7, 5 and 4 Å. The tilt axis is indicated by a dashed line. (b) Representative lattice lines (0, 3), (1, 5) and (2, 7) showing a good match between the experimentally observed reflection data and the calculated curves. The measured phases for lattice line (0, 3) were mostly 0 or 180°, indicating agreement with the $P42_12$ symmetry.
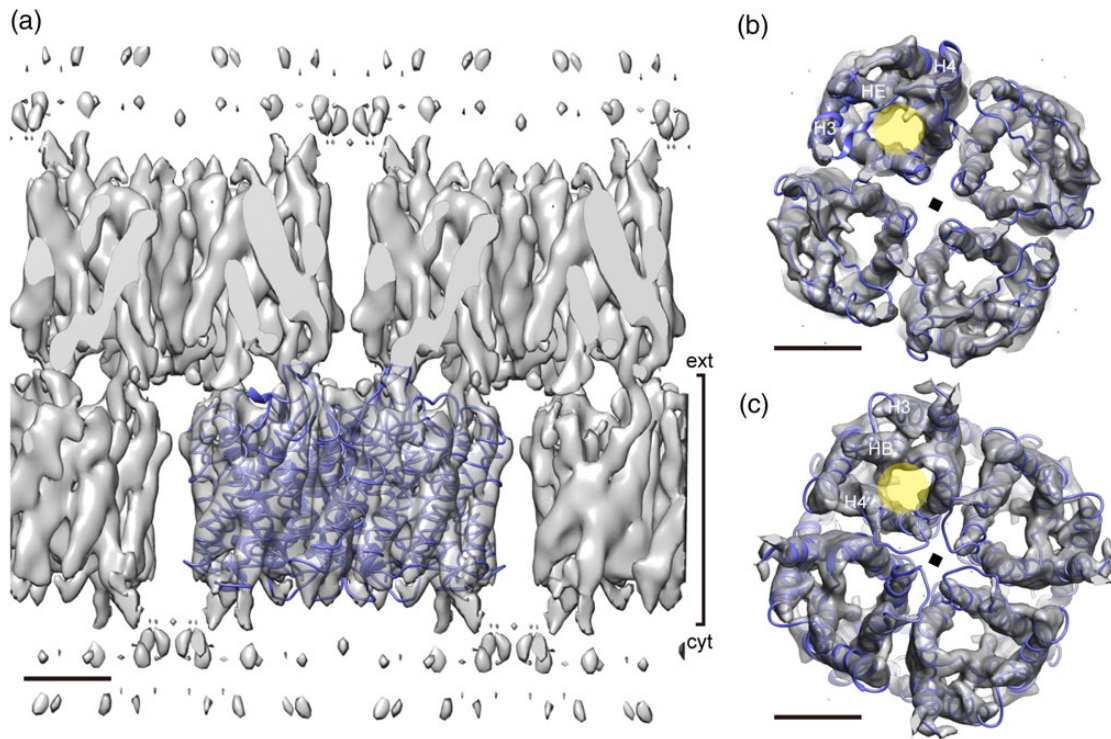
Fig. 2. Overviews of the map calculated from electron micrographs shown with a superimposed atomic model of AQP4 tetramer. Figures are viewed parallel with the membrane (a), from the extracellular side (b) and cytoplasmic side (c). The density map represented by the gray surface is contoured at 1.2σ and clearly shows six transmembrane helices in each monomer. Each AQP4 monomer is shown as a ribbon model, and one of four channel pores in a tetramer is indicated by a yellow transparent circle. The diamond symbol indicates the axis of 4-fold symmetry in the crystal. Scale bars represent 20 Å.
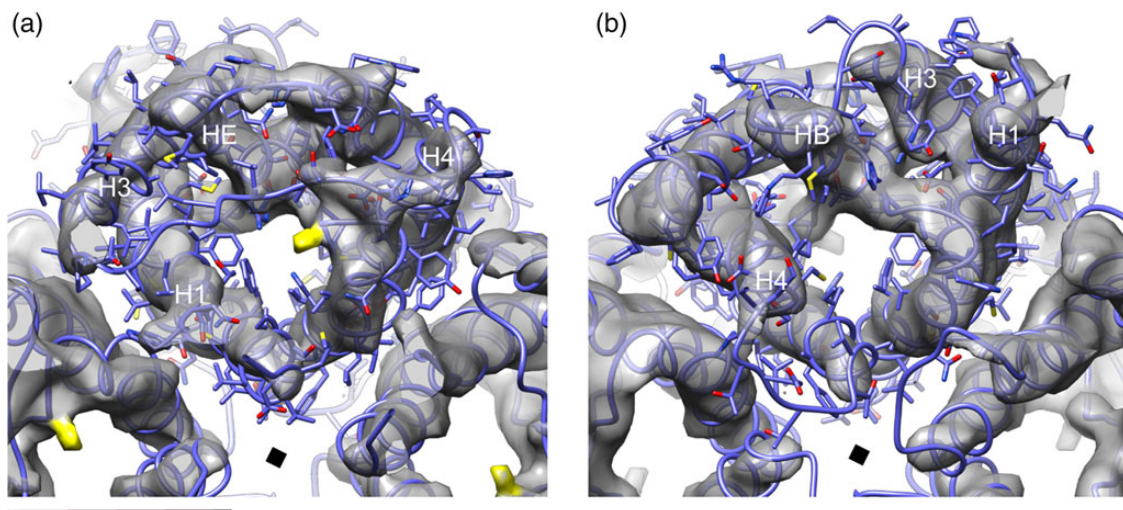
Fig. 3. Magnified views of the 5-Å map with a superimposed atomic model. Figures are viewed from the extracellular side (a), and cytoplasmic side (b). The density map represented by the gray surface is contoured at 1.2σ and the unexplained density identified with the fitting atomic model is shown in yellow and is located near the extracellular pore entrance. One of the tetramers is shown as a stick model, and the others are shown as a ribbon model. The diamond symbol indicates the axis of 4-fold symmetry in the crystal. Scale bar represents 20 Å.

cryo-EM density map of rAQP4M23 bound with AZA has been deposited in the Electron Microscopy Data Bank (http://www.emdatabank.org/) with accession code EMD-3214.

A model of rAQP4M23 was constructed from the high-resolution structure of rAQP4S180D (PDB: 2ZZ9) to replace Ser180 with Asp using COOT [42], and then fitted

to a density map using the 'fit in map' function of Chimera [41]. The AZA coordinate was downloaded from PubChem (CID: 1986). After roughly removing the geometry distortion of the ligand using Discovery Studio 4.5 (BIOVIA), the model was geometry-optimized using Gaussian 09 Rev. D.01 (Gaussian, Inc.) with the restricted Hartree-Fock model (RHF/6-31G(d)). The optimized coordinates and the

Table 1. Electron crystallographic data

Two-dimensional crystal	
Space group	$P42_12$
Lattice constants	$a = b = 69.1$ Å, $c = 160.0$ Å
	(assumed), $\gamma = 90.0°$
Number of images used	
Approximate tilt angle (°)	
0	6
20	38
45	50
60	47
Total	141
Resolution limit	
In membrane plane (Å)	5.0
Normal to membrane plane (Å)	5.7
Range of underfocus (Å)	5200–43 400
Number of observed reflections	16 595
Number of unique reflections	1006
Overall weighted phase residuals[a]	24.8
Overall weighted R-factor[a]	0.480

[a]Used reflections are better than IQ7.

model were used for a molecular docking simulation with AUTODOCK Vina [43]. The docking search area covered the whole extracellular cavity of AQP4 in a large box (30 × 30 × 30 Å) centered at the guanidino group of the Arg216 residue. Because the program predicted similar binding sites with a good score, only the three best high-scoring conformers are represented in Fig. 4 to elucidate the fitness of the ligand and the EM density map.

Results and discussion

Here we collected images of rAQP4M23 2D crystals and used them to calculate a 3D reconstruction at 5 Å resolution (Table 1 and Fig. 2). Almost all of the features of the density map were completely consistent with the previously determined atomic models of rAQP4M23 [35] and rAQP4M23S180D [36], because the AQP4 atomic model fit nicely with the whole density map using Chimera [41]. At first glance, the 5-Å map did not reveal a large density that could obstruct the channel entrance formed by the loop or the terminal domain of AQP4 (Fig. 2). Six transmembrane helices were clearly resolved at this resolution, and a water pathway was observed from the extracellular to the cytoplasmic side as being emphasized by transparent yellow in a pore region of the monomer (Fig. 2b and c). All densities except that near the extracellular pore entrance could be explained by the fitted atomic model showing that the water channel in AQP4 is likely to be in an open conformation.
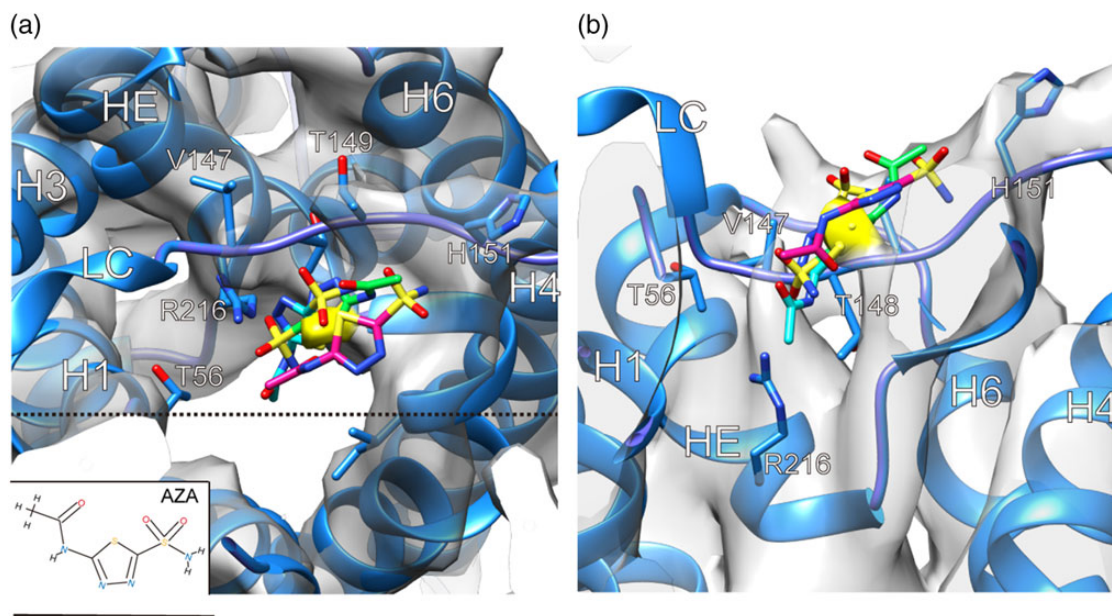
Fig. 4. Predicted conformations of AZA. (a) Figure is viewed from the extracellular side. (b) Sliced map viewed parallel to the membrane plane. The position of the sliced section is represented by the broken line in (a). The density map is represented as in Fig. 3. High energetically favorable conformations of AZA are shown as three favorable stick models (green: the most favorable) and AQP4 is shown as a ribbon model. LC indicates loop C between H3 and H4. In (a), inset shows the chemical structure of AZA. Scale bar represents 10 Å.
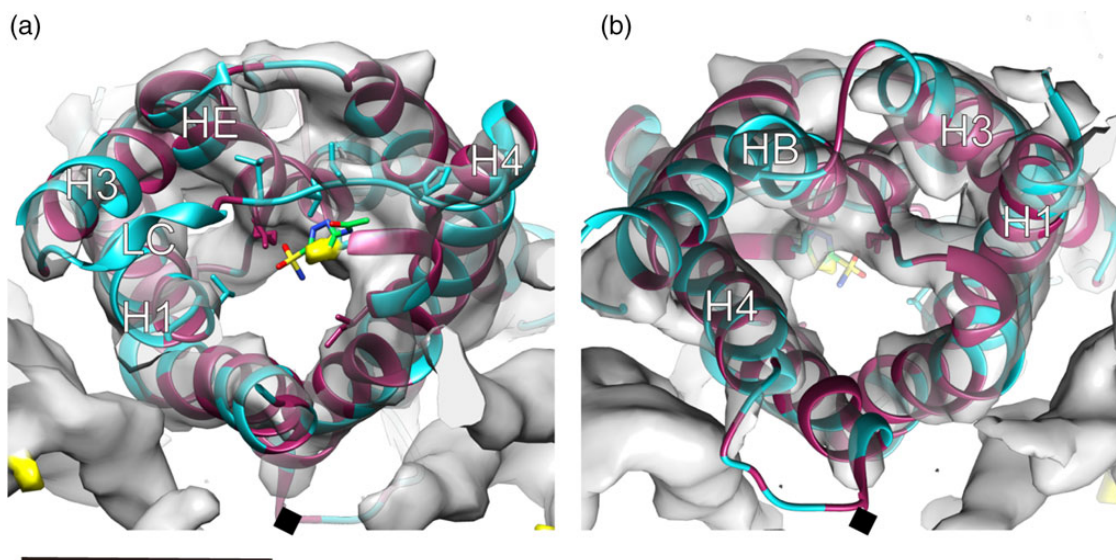
Fig. 5. The binding site mapping of sequence conservation. Figures are viewed from the extracellular side (a) and the cytoplasmic side (b). The density map is represented as in Fig. 3. The highest energetically favorable conformation of AZA is shown as a stick model and AQP4 is shown as a ribbon model. The mapping sequence conservation between rat AQP4 and human AQP1 is color-coded (maroon: identical, cyan: different). The diamond symbol indicates the axis of 4-fold symmetry in the crystal. Scale bar represents 20 Å.

Large conformational changes in AQP4 were not observed during AZA-induced reduction of AQP4 water permeability. The closed conformation of plant PIP2 induced by a divalent cation is accomplished by a large conformational change in loop D at the cytoplasmic side [17]. The inhibition of AQP4 by AZA therefore differs from that of PIP2.

The 5 Å map shows an interesting feature—a density on the extracellular side that protrudes into the channel pore entrance at 1.2σ (Fig. 3a). Based on the docked crystal structure, this density likely represents AZA, and the interaction of AZA and AQP4 suggests a direct role of AZA in the inhibition of the water permeability of AQP4. Furthermore, the center of the protrusion density is more than 1.35σ, which corresponds to the density of the helical region in the map. Such a significant feature is not observed in the density map at the cytoplasmic pore entrance, even when contoured at 0.8σ, which is close to the noise level. The clearly obstructing density at the limited resolution of our map leads us to propose that AZA is directly involved in water inhibition at the extracellular side. At the current resolution, however, the location of the loop region is sometimes unreliable, and thus we cannot exclude the possibility that the density represents a part of the extracellular loop of AQP4. The validity of the assignment conclusion must be confirmed by other methods.

To further confirm the assignment of the protruding density at the extracellular pore entrance, we performed a molecular docking simulation between AZA and AQP4. The predicted positions of the ligand located around the protruding density (Fig. 4). We selected the three most

energetically favorable conformations for which binding free energy ranged from −5.1 to −4.9 kcal mol^{-1}. All selected conformations occupied an almost identical position, suggesting that the protruding density is a thiadiazol ring of AZA (Fig. 3). The most favorable conformation of AZA was associated with 10 residues, including Thr56, Gly146, Val147, Thr148, Thr149, His151, Ile205, Gly209, Ala210 and Arg216 from H1, loop C, and HE (sticks in Fig. 4). In particular, the conserved Arg216 in HE comprises the ar/R constriction site and is thus crucial for allowing water molecules to permeate. The location of AZA seems to obstruct the ar/R constriction site of the channel pore by clogging it at the extracellular side.

Our previous water permeation experiments consistently revealed that AZA does not suppress the water permeability of AQP1, but clearly reduces AQP4 activity [34]. Considering the sequence alignment between AQP1 and AQP4, the conservation mapping to the AQP4 structure showed that most of the residues at the cytoplasmic side are more conserved than those at the extracellular side (Fig. 5). This tendency is stronger for the residues around loops C and HE. Because loops C and HE are located close to the water pore, changes in their interaction with AZA could influence the water permeability of AQP4. Together, these findings support the notion that water permeation through AQP4 is directly prevented by AZA binding at the extracellular side. Further structural and functional studies are needed to clarify the precise location of AZA binding and the precise mechanism of the inhibition of water passage.

In summary, our analysis of the crystal structure of AQP4 bound with AZA yields insights into the inhibitor binding conformation. Our electron crystallographic reconstruction provides a first glimpse of the inhibited AQP4 structure in the membrane. The AZA-binding location near the extracellular pore entrance visualized by the 5-Å map is in good agreement with the molecular docking simulation. This information will be beneficial toward designing a high-affinity AQP4 inhibitor.

References

1. Borgnia M, Nielsen S, Engel A, Agre P (1999) Cellular and molecular biology of the aquaporin water channels. *Annu. Rev. Biochem.* 68: 425–458.
2. Preston G M, Carroll T P, Guggino W B, Agre P (1992) Appearance of water channels in *Xenopus oocytes* expressing red cell CHIP28 protein. *Science* 256: 385–387.
3. Gonen T, Walz T (2006) The structure of aquaporins. *Q. Rev. Biophys.* 39: 361–396.
4. Tani K, Fujiyoshi Y (2014) Water channel structures analysed by electron crystallography. *Biochim. Biophys. Acta* 1840: 1605–1613.
5. Murata K, Mitsuoka K, Hirai T, Walz T, Agre P, Heymann J B, Engel A, Fujiyoshi Y (2000) Structural determinants of water permeation through aquaporin-1. *Nature* 407: 599–605.
6. de Groot B L, Grubmuller H (2001) Water permeation across biological membranes: mechanism and dynamics of aquaporin-1 and GlpF. *Science* 294: 2353–2357.
7. Rash J E, Yasumura T, Hudson C S, Agre P, Nielsen S (1998) Direct immunogold labeling of aquaporin-4 in square arrays of astrocyte and ependymocyte plasma membranes in rat brain and spinal cord. *Proc. Natl. Acad. Sci. USA* 95: 11981–11986.
8. Neely J D, Christensen B M, Nielsen S, Agre P (1999) Heterotetrameric composition of aquaporin-4 water channels. *Biochemistry* 38: 11156–11163.
9. Furman C S, Gorelick-Feldman D A, Davidson K G V, Yasumura T, Neely J D, Agre P, Rash J E (2003) Aquaporin-4 square array assembly: opposing actions of M1 and M23 isoforms. *Proc. Natl. Acad. Sci. USA* 100: 13609–13614.
10. Suzuki H, Nishikawa K, Hiroaki Y, Fujiyoshi Y (2008) Formation of aquaporin-4 arrays is inhibited by palmitoylation of N-terminal cysteine residues. *Biochim. Biophys. Acta* 1778: 1181–1189.
11. Moe S E, Sorbo J G, Sogaard R, Zeuthen T, Ottersen O P, Holen T (2008) New isoforms of rat aquaporin-4. *Genomics* 91: 367–377.
12. Sorbo J G, Moe S E, Ottersen O P, Holen T (2008) The molecular composition of square arrays. *Biochemistry* 47: 2631–2637.
13. Tong J, Briggs M M, McIntosh T J (2012) Water permeability of aquaporin-4 channel depends on bilayer composition, thickness, and elasticity. *Biophys. J.* 103: 1899–1908.
14. Nagelhus E A, Ottersen O P (2013) Physiological roles of aquaporin-4 in brain. *Physiol. Rev.* 93: 1543–1562.
15. Papadopoulos M C, Verkman A S (2007) Aquaporin-4 and brain edema. *Pediatr. Nephrol.* 22: 778–784.
16. Lennon V A, Kryzer T J, Pittock S J, Verkman A S, Hinson S R (2005) IgG marker of optic-spinal multiple sclerosis binds to the aquaporin-4 water channel. *J. Exp. Med.* 202: 473–477.
17. Tornroth-Horsefield S, Wang Y, Hedfalk K, Johanson U, Karlsson M, Tajkhorshid E, Neutze R, Kjellbom P (2006) Structural mechanism of plant aquaporin gating. *Nature* 439: 688–694.
18. Tornroth-Horsefield S, Hedfalk K, Fischer G, Lindkvist-Petersson K, Neutze R (2010) Structural insights into eukaryotic aquaporin regulation. *FEBS Lett.* 584: 2580–2588.
19. Daniels M J, Yeager M (2005) Phosphorylation of aquaporin PvTIP3;1 defined by mass spectrometry and molecular modeling. *Biochemistry* 44: 14443–14454.
20. Prak S, Hem S, Boudet J, Viennois G, Sommerer N, Rossignol M, Maurel C, Santoni V (2008) Multiple phosphorylations in the C-terminal tail of plant plasma membrane aquaporins: role in subcellular trafficking of AtPIP2;1 in response to salt stress. *Mol. Cell Proteomics* 7: 1019–1030.
21. Walz T, Fujiyoshi Y, Engel A (2009) The AQP structure and functional implications. *Handb. Exp. Pharmacol.* 190: 31–56.
22. Reichow S L, Gonen T (2008) Noncanonical binding of calmodulin to aquaporin-0: implications for channel regulation. *Structure* 16: 1389–1398.
23. Preston G M, Jung J S, Guggino W B, Agre P (1993) The mercury-sensitive residue at cysteine 189 in the CHIP28 water channel. *J. Biol. Chem.* 268: 17–20.
24. Niemietz C M, Tyerman S D (2002) New potent inhibitors of aquaporins: silver and gold compounds inhibit aquaporins of plant and human origin. *FEBS Lett.* 531: 443–447.
25. Yukutake Y, Tsuji S, Hirano Y, Adachi T, Takahashi T, Fujihara K, Agre P, Yasui M, Suematsu M (2008) Mercury chloride decreases the water permeability of aquaporin-4-reconstituted proteoliposomes. *Biol. Cell* 100: 355–363.
26. Yakata K, Tani K, Fujiyoshi Y (2011) Water permeability and characterization of aquaporin-11. *J. Struct. Biol.* 174: 315–320.
27. Verkman A S, Anderson M O, Papadopoulos M C (2014) Aquaporins: important but elusive drug targets. *Nat. Rev. Drug. Discov.* 13: 259–277.
28. Ma B, Xiang Y, Mu S M, Li T, Yu H M, Li X J (2004) Effects of acetazolamide and anordiol on osmotic water permeability in AQP1-cRNA injected *Xenopus oocyte*. *Acta. Pharmacol. Sin.* 25: 90–97.
29. Huber V J, Tsujita M, Yamazaki M, Sakimura K, Nakada T (2007) Identification of arylsulfonamides as aquaporin 4 inhibitors. *Bioorg. Med. Chem. Lett.* 17: 1270–1273.

30. Huber V J, Tsujita M, Kwee I L, Nakada T (2009) Inhibition of aquaporin 4 by antiepileptic drugs. *Bioorg. Med. Chem.* 17: 418–424.

31. Yang B, Kim J K, Verkman A S (2006) Comparative efficacy of HgCl2 with candidate aquaporin-1 inhibitors DMSO, gold, TEA + and acetazolamide. *FEBS Lett.* 580: 6679–6684.

32. Yang B, Zhang H, Verkman A S (2008) Lack of aquaporin-4 water transport inhibition by antiepileptics and arylsulfonamides. *Bioorg. Med. Chem.* 16: 7489–7493.

33. Søgaard R, Zeuthen T (2008) Test of blockers of AQP1 water permeability by a high-resolution method: no effects of tetraethylammonium ions or acetazolamide. *Pflugers. Arch.* 456: 285–292.

34. Tanimura Y, Hiroaki Y, Fujiyoshi Y (2009) Acetazolamide reversibly inhibits water conduction by aquaporin-4. *J. Struct. Biol.* 166: 16–21.

35. Hiroaki Y, Tani K, Kamegawa A, Gyobu N, Nishikawa K, Suzuki H, Walz T, Sasaki S, Mitsuoka K, Kimura K, Mizoguchi A, Fujiyoshi Y (2006) Implications of the aquaporin-4 structure on array formation and cell adhesion. *J. Mol. Biol.* 355: 628–639.

36. Tani K, Mitsuma T, Hiroaki Y, Kamegawa A, Nishikawa K, Tanimura Y, Fujiyoshi Y (2009) Mechanism of aquaporin-4's fast and highly selective water conduction and proton exclusion. *J. Mol. Biol.* 389: 694–706.

37. Fujiyoshi Y, Mizusaki T, Morikawa K, Yamagishi H, Aoki Y, Kihara H, Harada Y (1991) Development of a superfluid helium stage for high-resolution electron microscopy. *Ultramicroscopy* 38: 241–251.

38. Fujiyoshi Y (1998) The structural study of membrane proteins by electron crystallography. *Adv. Biophys.* 35: 25–80.

39. Crowther R A, Henderson R, Smith J M (1996) MRC image processing programs. *J. Struct. Biol.* 116: 9–16.

40. Henderson R, Baldwin J M, Downing K H, Lepault J, Zemlin F (1986) Structure of purple membrane from *Halobacterium halobium*: recording, measurement and evaluation of electron micrographs at 3.5 Å resolution. *Ultramicroscopy* 19: 147–178.

41. Pettersen E F, Goddard T D, Huang C C, Couch G S, Greenblatt D M, Meng E C, Ferrin T E (2004) UCSF chimera—a visualization system for exploratory research and analysis. *J. Comput. Chem.* 25: 1605–1612.

42. Emsley P, Cowtan K (2004) Coot: model-building tools for molecular graphics. *Acta. Crystallogr. D. Biol. Crystallogr.* 60: 2126–2132.

43. Trott O, Olson A J (2010) AutoDock Vina: improving the speed and accuracy of docking with a new scoring function, efficient optimization, and multithreading. *J. Comput. Chem.* 31: 455–461.